Journal of Non-Crystalline Solids 506 (2019) 68–79

Contents lists available at ScienceDirect

Journal of Non-Crystalline Solids

journal homepage: www.elsevier.com/locate/jnoncrysol

Effect of gadolinium on magnetic circular dichroism and electron magnetic resonance of ε-Fe_2O_3 nanoparticles formed in borate glasses

I. Edelman[a,*], J. Kliava[b], O. Ivanova[a], R. Ivantsov[a], D. Velikanov[a,c], V. Zaikovskii[d], E. Petrakovskaja[a], Y. Zubavichus[e], S. Stepanov[f]

[a] Kirensky Institute of Physics, Federal Research Center KSC SB RAS, 660036 Krasnoyarsk, Russia
[b] LOMA, UMR 5798 Université de Bordeaux-CNRS, 33405 Talence cedex, France
[c] Siberian Federal University, 660041 Krasnoyarsk, Russia
[d] Boreskov Institute of Catalysis, Siberian Branch of RAS, 630090 Novosibirsk, Russia
[e] NRC "Kurchatov Institute", 123182 Moscow, Russia
[f] Vavilov State Optical Institute, 199053 St.-Petersburg, Russia

ARTICLE INFO

Keywords:
Iron oxides
ε-Fe_2O_3
Borate glasses
Nanoparticles
Magnetic circular dichroism
Electron magnetic resonance

ABSTRACT

A remarkable characteristic of borate glasses is the ability of forming magnetic nanoparticles at low doping with transition element oxides. We have studied structure and magnetic properties of iron oxide nanoparticles formed in borate glasses, in particular, concentration and temperature dependences of magnetic circular dichroism (MCD) and electron magnetic resonance (EMR) spectra. A series of glasses of molar composition 22.5K_2O-22.5Al_2O_3–55B_2O_3 doped with 1.5 mass % of Fe_2O_3 and different contents of Gd_2O_3 from 0.1 to 1.0 mass % was prepared using a conventional melt quenching technique and subjected to an additional thermal treatment. The whole set of results allows to identify the predominant magnetic phase in these glasses as ε-Fe_2O_3 nanoparticles, with a considerable part of iron ions substituted by gadolinium. Analysis and computer simulations of the EMR spectra allow separating the contribution of electron paramagnetic resonance of diluted iron ions and together with the temperature dependences of magnetization demonstrate a superparamagnetic character of the nanoparticle magnetism.

1. Introduction

Glass technology, being one of the oldest ways of creating materials, is still in high demand due to its facility of combining different elements, virtually unlimited variability and low production cost. In particular, in the context of the present study most interesting are works concerning the formation of magnetically ordered nanoparticles in glasses doped with transition or/and rare earth oxides [1–13]. As a rule, in order to obtain magnetic nanoparticles, rather high contents of transition metal oxides, most frequently Fe_2O_3, are introduced in the glass composition. The structure and magnetic properties of nanoparticles formed in the glasses greatly depend on technological conditions, basic glass compositions and on the nature and concentration of paramagnetic dopants. For instance, magnetite, Fe_3O_4 nanoparticles are formed in borosilicate and aluminoborosilicate glasses containing 17.5 mass % of Fe_2O_3 together with low amounts of Cr_2O_3 or P_2O_5 [13,14]. In 30SiO_2-8B_2O_3-$x$$Al_2O_3-40Fe_2O_3$-(22 − x) SrO glasses (x = 0, 3, 6 and 9 mass %), Fe_3O_4 nanoparticles spontaneously arise, with magnetic parameters depending on x [15]. Fe_3O_4 nanocrystals are also formed in glasses of molar compositions 33.3CaO-4.9Na_2O-17.1Fe_2O_3–44.7B_2O_3 [5] and (24-y)Na_2O-$y$$Al_2O_3-14B_2O_3-37SiO_2-25Fe_2O_3$ with y = 8 to 16 [16], with size and properties depending on y. Fe_3O_4 nanoparticles formed in the glass of molar composition 27.4CaO-42.8SiO_2–6.1B_2O_3–23.7Fe_2O_3 are surrounded with a nonmagnetic shell with distorted crystal structure [17]. Nanocrystals containing both hematite, α-Fe_2O_3 and magnetite, Fe_3O_4 phases have been detected in 16Na_2O-10CaO-49SiO_2-25Fe_2O_3 glasses [18]. A formation of maghemite, γ-Fe_2O_3 nanoparticles in a number of glasses has been reported [19].

ε-Fe_2O_3 nanoparticles hold a special place among other iron oxides as an advanced nanomaterial exhibiting giant coercivity, millimetre-wave ferromagnetic resonance and strong magneto-electric coupling [20]; therefore they have being extensively studied over the last decade [21–25]. The ε-Fe_2O_3 polymorphous phase is not found in nature (except in heated archaeological materials [26]). This phase can be considered as an intermediate one between γ- and α-Fe_2O_3, and it is usually

* Corresponding author.
E-mail address: ise@iph.krasn.ru (I. Edelman).

https://doi.org/10.1016/j.jnoncrysol.2018.12.006
Received 29 October 2018; Received in revised form 21 December 2018; Accepted 21 December 2018
Available online 23 January 2019
0022-3093/

found together with the two latter polymorphs [21]. Depending on the preparation method, the temperature of ε- to α-Fe_2O_3 transformation falls within the range of 500 to 750 °C. Because of the agglomeration of nanoparticles, the transition can occur directly from γ- to α-Fe_2O_3 [20]. Therefore, the ε-Fe_2O_3 phase is usually obtained as nanoparticles dispersed in matrices preventing their agglomeration. However, some authors, e.g., Sivkov et al. [27] have reported a successful synthesis of ε-Fe_2O_3 powdered samples.

The structure and properties of ε-Fe_2O_3 are markedly different from those of γ- and α- polymorphs. While γ-Fe_2O_3 crystallizes in spinel structure with Fe^{3+} ions in octahedral and tetrahedral sites, and α-Fe_2O_3 has rhombohedral structure with Fe^{3+} ions in octahedral sites [28], the situation with ε-Fe_2O_3 is more complicated. In earlier works, Schrader and Buttner [29] have identified its structure as monoclinic with $a = 12.97$, $b = 10.21$, $c = 8.44$ (in Å) and $\beta = 95.66^{\circ}$. Dézsi and Coey [30] report a simpler structure; nevertheless, they also refer to it as ε-Fe_2O_3 subjected to disorder effects. Tronc, Chanéac and Jolivet [21] have shown that high-temperature heat treatment of γ-Fe_2O_3 nanoparticles dispersed in silica xerogel gives rise to the formation of ε-Fe_2O_3 nanoparticles with an average diameter about 30 nm, having orthorhombic structure with $a = 5.095$, $b = 8.789$ and $c = 9.437$ Å. This phase is shown to be isomorphous with $GaFeO_3$ [31], $AlFeO_3$ [32], and κ-Al_2O_3 [33], where Fe^{3+} ions occupy four different sites: an undistorted octahedral (O1), two distorted octahedral (O2 and O3), and a distorted tetrahedral (T) sites. Later, Kelm and Mader [34] have specified the structure of ε-Fe_2O_3 nanoparticles obtained by thermal decomposition of nontronite (a clay mineral) and subsequent isolation of ferric oxide by leaching silicate phases. These authors have also found for ε-Fe_2O_3 an orthorhombic structure of $Pna2_1$ space group with $a = 5.072$, $b = 8.736$, $c = 9.418$ (in Å) and $\alpha = \beta = \gamma = 90^{\circ}$, with all four Fe^{3+} sites exhibiting different degrees of distortion. The less distorted octahedral site, denoted as O1 [21], is often referred to as an "undistorted" one. The average distances between the central Fe^{3+} ion and surrounding oxygens have been determined for all four sites [34]: 2.10, 1.97, 2.04 and 1.85 Å for O1, O2, O3 and T sites, respectively. The corresponding magnetic moments are: $\mu(O1) = 3.7$, $\mu(O2) = -3.9$, $\mu(O3) = 3.9$ and $\mu(T) = -2.4$ (in Bohr magnetons) [35], so that the net magnetization is due to the difference between those of O1 and T sublattices, similarly to ferrite spinels.

The procedure of preparing a particular iron oxide phase is extremely sensitive to technological conditions. Jin, Ohkoshi and Hashimoto [36] have synthesized iron oxide in porous silica matrix by combining reverse-micelle and sol-gel techniques at different temperatures: 900, 1000 and 1100 °C, and obtained magnetization curves for γ-, ε- and α-Fe_2O_3 with coercivity about 0.5 T, 2 T and without hysteresis, respectively. Gich et al. [22,37,38] have synthesized ε-Fe_2O_3 nanoparticles about 25 nm in diameter by sol-gel technique and subsequent high-temperature treatment. Similarly to the findings of Tronc, Chanéac and Jolivet [21], an orthorhombic nanoparticle lattice has been found, with the parameters $a = 5.098(2)$, $b = 8.785(3)$ and $c = 9.468(2)$ Å only slightly different from those quoted by the former authors. The nanoparticle coercivity at room temperature was high, about 2.0 T, but substantially decreased upon cooling. The nanoparticle magnetic structure has been identified as a collinear ferrimagnet above 150 K and a square-wave incommensurate structure below 80 K. The transformation between these two structures has been identified as a second-order phase transition involving subtle structural changes, mostly in the tetrahedral and one of the octahedral Fe^{3+} sites [22,37]. Kohout et al. [35] have synthesized ε-Fe_2O_3 nanoparticles with an average diameter about 25 nm and the lattice parameters $a = 5.105(1)$, $b = 8.800(2)$ and $c = 9.476(2)$ Å, stabilized in amorphous silica matrix by sol-gel technique. These authors have also detected a change of magnetic state below 150 K, described as a two-step transition, the first step in the range of 153 to 130 K being related to a reorientation of local magnetic moments in magnetic sublattices, and the second step in the range of 130 to 100 K being ascribed to an intermediate spin – high spin transition of Fe^{3+} ions in the tetrahedral sublattice.

A number of authors have shown that the magnetic characteristics of ε-Fe_2O_3 nanoparticles greatly depend on their size, specific substrate as well as on technological parameters. For instance, a variation of the annealing temperature in the range of 900 to 1050 °C and of the annealing time has resulted in reducing the coercivity of ε-Fe_2O_3 nanoparticles prepared by sol-gel technique from 1.54 to 0.06 T [39]. Sol-gel prepared γ- and ε-Fe_2O_3 nanoparticles of 10 to 80 nm in size had the coercivity lower than 0.24 T; meanwhile, the saturation has not been reached in the magnetizing field up to 2 T [40]. Substantial changes have been reported in magnetic characteristics of fine (3.4 nm) ε-Fe_2O_3 nanoparticles prepared by impregnating silica gel and aluminium oxide with $FeSO_4$ solutions [23–25,41]. Coercivity of ε-Fe_2O_3 particles of sizes ranging from 7 to 15 nm, embedded in SiO_2 films, was 0.009 T [42].

The results outlined above demonstrate the crucial role of synthesis conditions in the formation of iron oxide nanoparticles of different polymorph phases, ε-Fe_2O_3 in particular.

Recently, we have reported a new possibility of obtaining ε-Fe_2O_3 nanoparticles: their spontaneous formation in the course of devitrification and subsequent thermal treatment of Al_2O_3-K_2O-B_2O_3 glasses co-doped with low contents of Fe_2O_3 and Gd_2O_3 [43–45]. However, the role of gadolinium in the nanoparticle formation and its effect on the nanoparticle properties has not been elucidated in our previous works. The purpose of the present work is a comprehensive study of these issues in glasses with different Gd_2O_3 contents, using principally two experimental techniques: magnetic circular dichroism (MCD) and electron magnetic resonance (EMR). As far as MCD and EMR are due to fundamentally similar physical effects, these techniques are expected to yield consistent and complementary characterization of glasses containing magnetic nanoparticles [46]. We are using the term EMR because, as will be seen below, in our samples both magnetic resonances due to diluted paramagnetic ions and to magnetically ordered phases are simultaneously observed. In order to separate these contributions, we have carried out detailed computer simulations of experimental EMR spectra, using an original approach described below.

Prior to MCD and EMR studies, the samples were characterized by structural and static magnetic measurements. In order to provide a comprehensive analysis of our results concerning ε-Fe_2O_3 nanoparticles formed in borate glasses, we have used certain structural and EMR data reported in our previous publications [43–45].These data are shown in Figs. 2, 3 and 9 a.

2. Materials and methods

Glasses of basic composition $22.5K_2O$-$22.5Al_2O_3$–$55B_2O_3$ were synthesized using conventional glass-making technique. Prior to the synthesis, 1.5 mass % of Fe_2O_3 was loaded in the charge together with 0.1, 0.2, 0.3, 0.4, 0.6, and 1.0 mass % of Gd_2O_3 relative to basic glass composition (samples 1 to 6, respectively). A low (less than 0.1 mass %) Cr_2O_3 content was added to all compositions. The mixtures were melted at 1100–1300 °C under oxidizing conditions. The melts were poured onto steel sheets and cooled in air to 380 °C. Then the glass plates were subjected to an additional thermal treatment during 2 h at 560 °C in the same conditions.

The particles formed in the glasses were visualized by an electron microscope JEM-2200FS (JEOL Ltd) operating in high resolution and high-angle annular dark-field scanning (STEM-HAADF) transmission modes. Energy-dispersive X-ray analysis (EDX) was used to identify chemical elements in the glass composition. Interplanar distances in the nanoparticle lattice were measured by Fast Fourier transform (FFT) with Digital Micrograph 3.3.1 (Gatan Ltd). For electron microscopic studies the samples were finely ground, dispersed in ethanol, deposited onto perforated carbon substrates attached to a standard copper grid, and placed into the microscope UHV chamber.

The XRD analysis was carried out at the "Structural Materials Science" beamline in the Kurchatov Synchrotron Radiation Centre

(Moscow, Russia). The X-ray diffraction data were acquired in transmission (Debye–Scherer) mode at the wavelength of 0.696585 Å using a Fujifilm Imaging Plate as a 2D detector.

Magnetic properties of the samples were studied with a Superconducting Quantum Interference Device (SQUID) magnetometer in the temperature range of 78 to 300 K in the magnetizing field up to 2 T.

The MCD was recorded in the energy range of 1.2 to 2.9 eV at different temperatures between 90 and 300 K in magnetic fields 0.35 and 1.3 T. The MCD measurement accuracy was about 10^{-4}, and the spectral resolution was from 2.5 to 6.2 × 10^{-3} eV, depending on the spectral range.

The EMR spectra were recorded in the X band (ca. 9.5 GHz) at 300 and 120 K with a Bruker EMX spectrometer equipped with an ER4112HV variable-temperature unit.

The spectra have been computer simulated, as described in detail in 3.4.2 section.

The magnetic field was measured with accuracy of ± 0.0005, ± 0.0002 and ± 0.0001 T in SQUID, MCD and EMR experiments, respectively. The temperature measurement accuracy was ± 2 K for all three techniques.

3. Results

3.1. Transmission electron microscopy

Inclusions of density different from that of the basic matrix are clearly seen in TEM images of all samples. The STEM-HAADF images of samples 1 and 6, with the lowest and the highest Gd_2O_3 content, are shown in Figs. 1 a and 2 a, respectively. The inclusions are compact particles about 30–50 nm in size as well as aggregates of smaller particles with sizes from 5 to 10 nm. Interplanar distances in the nanoparticle lattice obtained with FFT analysis, 0.2518–0.2501, 0.2284–0.2224 and 0.2032–0.1981 nm, are indicative of ε-Fe_2O_3 structure [21,30]. Indeed, these distances are in close agreement with those reported for ε-Fe_2O_3, 0.2541, 0.2237, 0.1992 [21] and 0.2529, 0.2229, 0.1971 [47].

The results of elemental mappings are shown in Figs. 1 b, c, d and 2 b, c, d for samples 1 and 6, respectively. The spatial distributions of atoms of the basic glass are nearly uniform throughout the samples, with visible “pits” at the location of the nanoparticles. Iron also is nearly uniformly distributed outside the nanoparticles but considerably concentrated inside them (Figs. 1 c and Fig. 2 c). In sample 6, iron mainly occurs in the regions where larger particles are located (Fig. 2 c), and its distribution outside these region is no more uniform.

In samples with lower Gd_2O_3 contents, no condensation of gadolinium is observed (Fig. 1 d). At higher Gd_2O_3 contents the distribution of gadolinium becomes similar to that of iron (Fig. 2 d). Seemingly, at higher Gd_2O_3 contents gadolinium is mainly included into the nanoparticles.

The X-ray diffraction patterns for all samples show the same weak reflections in the angular range of 22 to 29°., see Fig. 3. At lower angles, the reflections arising from the nanoparticles are masked by a background diffraction from the glass matrix. The angular positions of reflections coincide with those reported for ε-Fe_2O_3 nanoparticles prepared by different techniques [21,30].

One might suppose that nanophases of other iron oxides, e.g., Fe_3O_4, α-Fe_2O_3 or γ-Fe_2O_3 could also be formed in the gadolinium-containing glasses. The XRD patterns of the first and the second compounds noticeably differ from those of ε-Fe_2O_3 [48–50]; however, there is more similarity between the XRD patterns of ε-Fe_2O_3 and γ-Fe_2O_3 [51]. Indeed, more or less intense reflexes (134), (135) and (330) seen in Fig. 3 are in the same angular range 22.5 to 27 degrees as (422), (511) and (330) reflexes of γ-Fe_2O_3. Nevertheless, the angular distances between the reflexes and their relative intensities are noticeably different in these two cases. Thus, the XRD data confirm the identification of the predominant magnetic phase in the actual case as ε-Fe_2O_3.

3.2. Static magnetization

The dependence of the magnetization on the magnetizing field for this series of glasses has been reported earlier [43]. At room temperature, the magnetization curves show hysteresis loops with temperature-independent coercivity H_c, of 0.05 to 0.07 T. Rather low and temperature-independent H_c values are in contrast with the findings for ε-Fe_2O_3 nanoparticles reported by certain authors, viz., a very high, about 2 T, room-temperature coercivity, sharply decreasing at lower temperatures [21,22,36]. Such characteristics of coercivity have been observed by Gish et al. [22]. for ε-Fe_2O_3 nanoparticles produced by sol-gel technique, about 25 nm in size with narrow size distribution and high crystallinity, and have been related to high room-temperature magnetic anisotropy and its complicated changes with the decrease of temperature. On the other hand, for fine ε-Fe_2O_3 nanoparticles Dubrovskiy et al. [41] have reported rather low room-temperature coercivity, about 0.1 T, without noticeable changes with the decrease of temperature. The latter authors have explained these characteristics by surface effects, unsaturated chemical bonds at the surface resulting in a transformation of the magnetic state of the nanoparticle surface shell from ferromagnetic to paramagnetic one.

One can see that there is a large divergence in the literature concerning the coercivity of ε-Fe_2O_3 nanoparticles; this can be related to differences both in particle morphology and in characteristics of their surface. In our case, the situation can be even more complicated, since gadolinium ions can enter inside the nanoparticles and other glass matrix components can be included in the nanoparticle shell.

The temperature dependence of magnetization, M of fine magnetic nanoparticles can be described in terms of the theory of superparamagnetism [52]. According to the latter, one should expect different temperature dependences of M for different cooling regimes: with or without an applied magnetic field (field-cooled, FC and zero-field cooled, ZFC regimes, respectively). Fig. 4 shows the temperature dependences of M in both regimes for sample 6 measured in the magnetizing field of 0.06 T. For this sample, the FC and ZFC curves diverge at ca. 150 K; however, the maximum of the ZFC curve, characteristic of

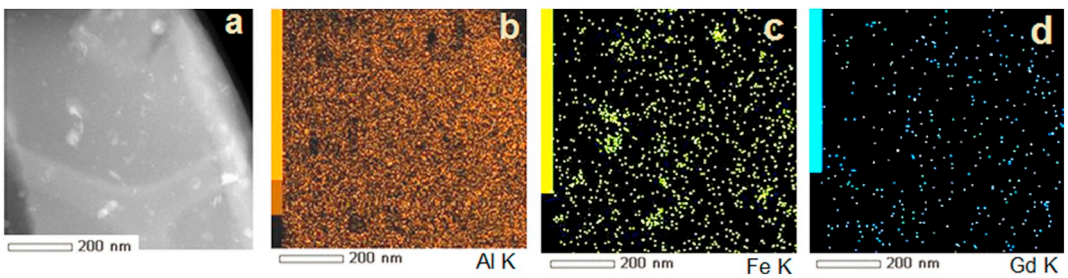

Fig. 1. STEM-HAADF image of a fragment of sample 1(a) EDX elemental mappings over the entire fragment for aluminium, iron, and gadolinium (b, c, d, respectively).

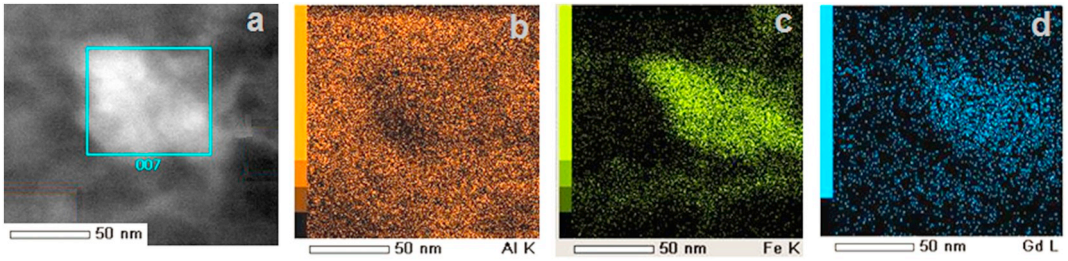

Fig. 2. STEM-HAADF image of a fragment of sample 6. The region of the particle is singled out with square (a). EDX elemental mappings over the entire fragment for aluminium, iron, and gadolinium (b, c, d), respectively.

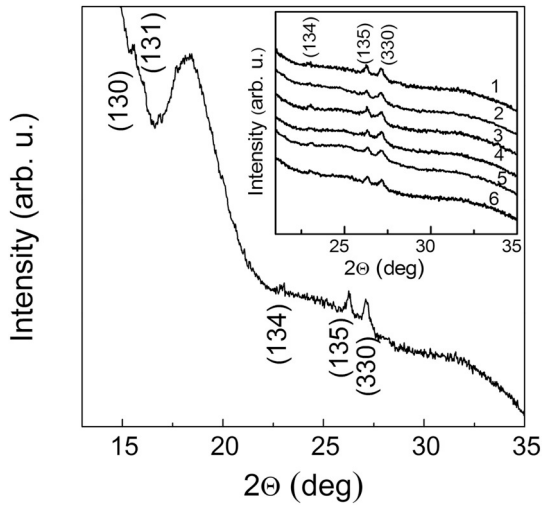

Fig. 3. XRD patterns for sample 1 measured at the wavelength of 0.696585 Å. The inset shows the XRD patterns for all samples measured at the same wavelength in a narrower angular range; the curve numbers are the sample numbers. The indices of some ε-Fe_2O_3 reflections are shown.

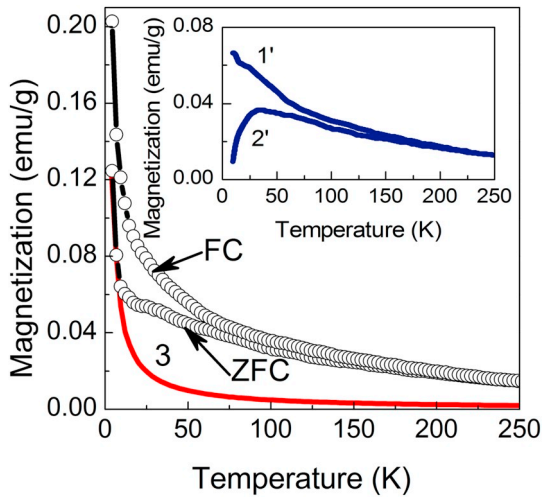

Fig. 4. Experimental FC (1) and ZFC (2) magnetization curves for sample 6 in the magnetizing field of 0.06 T and the calculated paramagnetic contribution due to diluted Fe^{3+} and Gd^{3+} ions (3). The inset shows the FC (1′) and ZFC (2′) curves after subtracting this contribution.

superparamagnetic nanoparticles, is not observed, and only a minor bend is seen near 50 K. Possibly, this maximum is masked by sharp magnetization increase at low temperatures due to contributions of diluted iron and gadolinium ions, see Figs. 1 and 2. These contributions have been estimated according to the following expression:

$$M = M_0 B_S(y) = M_0\left(\frac{2S+1}{2S}\mathrm{cth}\frac{2S+1}{2S}y - \frac{1}{2S}\mathrm{cth}\frac{y}{2S}\right) \quad (1)$$

where $M_0 = Ng\mu_B S$, $B_S(y)$ is the Brillouin function of $y = \frac{Sg\mu_B H}{kT}$, S is the electron spin of an ion, k is the Boltzmann constant, N is the number of atoms per unit volume, g is the Landé factor, μ_B is the Bohr magneton, T is the temperature and H is the magnetizing field.

On the basis of the elemental mapping, see Fig. 2, we assume that in sample 6 50% of Gd^{3+} and 25% of Fe^{3+} ions are diluted in the glass matrix. For Fe^{3+} S = 5/2 and for Gd^{3+} S = 7/2, and g = 2.0 for both ions. The calculated curve for the sum of contributions of the diluted Fe^{3+} and Gd^{3+} ions is shown in Fig. 4 (curve 3). Subtracting this curve from the experimental FC and ZFC curves (1 and 2, respectively), we obtained the FC and ZFC curves for the nanoparticles; see inset in Fig. 4. Note that the ZFC curve clearly exhibits a maximum about 35 K. Interestingly, a maximum about 20 K in the ZFC curve was observed for ε-Fe_2O_3 nanoparticles with average diameter of 3 nm embedded in silica gel matrix [41]. This maximum can be indicative of the transition of the magnetic state of the nanoparticles from the superparamagnetic to the blocked one. The occurrence of the wide maximum in the ZFC curve characteristic of superparamagnetic nanoparticles is similar to that reported by López-Sánchez et al. [42] and can be explained by a large spread in the nanoparticle sizes.

A comparison of the magnetization of our glasses with those of other iron oxide nanophases is not straightforward because of uncertainty in determination of the nanoparticle mass. More instructive is the temperature dependence of the magnetization; indeed, it allows to rule out any significant contribution of α-Fe_2O_3. Indeed, the latter near 270 K undergoes a transition from a canted to a collinear antiferromagnetic, so that its net magnetization drops to zero; such behavior has not been observed in our glasses. On the other hand, the almost temperature-independent coercivity of the latter makes highly improbable an involvement of Fe_3O_4 or γ-Fe_2O_3; indeed, the coercivity of nanoparticles of these compounds is strongly temperature-dependent [51,53].

3.3. MCD spectra

The MCD spectra in the range of 1.2 to 3.0 eV are shown in Fig. 5 for samples 2 and 6. For all other samples, the spectra in the range of 2.0 to 3.0 eV are identical in shape. The higher energy part of the spectrum (above 1.8 eV) is characterized by a broad maximum consisting of several overlapping features. (A lower-energy part of the spectrum will be discussed in detail below). The shape of the MCD spectra has been the main argument allowing to rule out a formation of Fe_3O_4 nanoparticles in iron- and gadolinium-containing borate glasses; indeed, the MCD spectrum of this compound is completely different [50].

The integral MCD intensity in the range of 2.0 to 3.0 eV, determined as the area under the spectral curve, depends on Gd_2O_3 contents in the glass. The minimum intensity occurs for sample 1 with the lowest Gd_2O_3 content; for sample 2 it abruptly increases and for samples with higher Gd_2O_3 contents it decreases albeit more gradually (Fig. 6). This behaviour can be understood assuming that gadolinium plays a certain role in phase separation of the glasses, contributing to the formation of

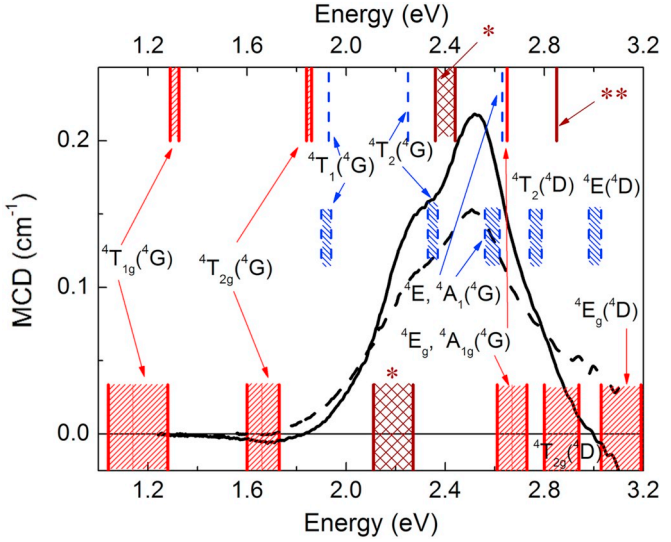

Fig. 5. Experimental MCD spectra of samples 2 (solid line) and 6 (dashed line) recorded at 300 K in the magnetic field of 1.3 T. The hatched bars show energy ranges of the CF d-d transitions in diluted Fe^{3+} ions taken from literature [54]: the oblique-hatched (red online) bars in the bottom, for octahedral sites in $ZnGa_2O_3$, $Li_{0.5}Ga_{2.5}O_4$ and $Y_3Ga_5O_{12}$; the oblique-hatched (blue online) bars in the middle, for tetrahedral sites in $Li_{0.5}Ga_{2.5}O_4$ and $Y_3Ga_5O_{12}$. The solid and dashed bars in the top (red and blue online) refer respectively to the transitions in octahedral and tetrahedral sublattices of γ-Fe_2O_3. The cross-hatched bars (brown online) show the positions of pair transitions: $2(^6A_{1g}) \rightarrow 2(^4T_{1g}(^4G))$ and $2(^6A_{1g}) \rightarrow 2(^4T_{1g} + {}^4T_{2g})$. These transitions are also marked with one and two asterisks, respectively. The bar widths show the data dispersal for different compounds. (For interpretation of the references to colour in this figure legend, the reader is referred to the web version of this article.)

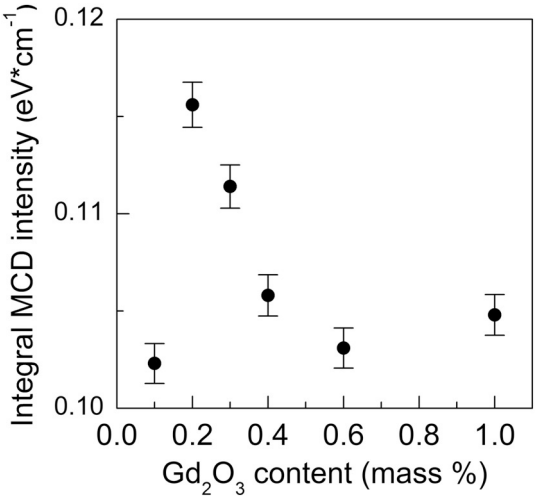

Fig. 6. Integral MCD intensity vs. Gd_2O_3 contents, calculated as the area under the spectral curves in the range of 2.0 to 3.0 eV. The error bars show the accuracy of measurements.

magnetic nanoparticles, see the discussion below. As a consequence, an initial increase in Gd_2O_3 content (samples 1 to 2) results in an increase of the total number or total volume of nanoparticles and therefore, of the MCD intensity. However, a further increase in Gd_2O_3 content leads to decreasing the MCD intensity. This can be understood assuming that Gd^{3+} ions are partially substituting Fe^{3+} ions in the nanoparticles, and as a result, the magnetization and, therefore, the MCD intensity of the latter is lowered.

In the lower-energy range (below 2.0 eV) the MCD spectra shape depends on Gd_2O_3 content, see Fig. 7. At room temperature, the MCD spectra of all samples can be divided into two groups, see Fig. 7 a. For samples 1 to 3, the dominant feature in the range of 1.2 to 1.8 eV is a broad asymmetric negative peak, and the MCD sign changes to positive below 1.4 eV. With the decrease of temperature to 90 K, the amplitude of the negative peak does not considerably change but the peak narrows and becomes more symmetric, and the point of the MCD sign change shifts to 1.55 eV. Besides, the broad positive peak in the low-energy range considerably increases in intensity. However, the behaviour is quite different for samples 4 to 6, in which case, instead of the broad negative peak, a more complex structure is observed in this spectral range, i.e., a positive and a negative peak centred at 1.63 and 1.71 eV, respectively, together forming a unique S-shape feature, and a broad negative peak centred at 1.45 eV, probably consisting of several components. With the decrease of temperature, the intensities of the latter peaks decrease, so that at 90 K only two smooth features remain in this part of the spectrum, see Fig. 7 b.

With the decrease of temperature, MCD in the spectral range of 2.0 to 3.0 eV considerably increases for all samples, e.g., see Fig. 8 for sample 2. With the decrease of temperature from 270 to 100 K, the integral MCD intensity for this sample, calculated as the area under the spectral curve in the range of 2.0 to 3.0 eV, increases almost twice. This behaviour correlates with the increase of magnetization in this temperature range, e.g., see Fig. 4; on the other hand, it is in stark contrast with only a slight change in the MCD intensity observed in the same temperature range for γ-Fe_2O_3 [51].

Before discussing the effect of gadolinium on the MCD spectra characteristics, the latter should be related with possible electron transitions in the magnetic ions. In general, in the spectral range in question two types of transitions are considered for Fe^{3+} ions: crystal-field (CF) d-d transitions between the ground and excited states of Fe^{3+} in octahedral or tetrahedral sites [54,55] and pair transitions, i.e. simultaneous excitation of exchange-coupled pairs of Fe^{3+} ions [54,56–58].

As concerns CF f-f transitions in Gd^{3+} ions, the lowest excited 4f level in Gd^{3+} lies 3.96 eV above the ground level, and the fundamental absorption edge in compounds containing Gd^{3+} in oxygen surroundings lies near 5.2 eV [59], well beyond the spectral range in question. Thus, the observed MCD can only be due to electron transitions in Fe^{3+} ions. The d-d transitions are usually considered in terms of the Tanabe-Sugano diagrams [60]. For each electron configuration, the excited level energies depend on the distances between the central ion and its ligands. In the actual case, Fe^{3+} ions occupy four different sites, see Introduction.

It is well known that Fe^{3+}–O^{2-} distances in the same coordination are very close for all oxides, including the cases where Fe^{3+} is an impurity (Table 1). Therefore, different features in our recorded MCD spectra can be assigned to particular electron transitions in accordance with the identification [54] of absorption spectra of several compounds where Fe^{3+} ions occupy either only octahedral sites ($ZnGa_2O_3$, $Li_{0.5}Ga_{2.5}O_4$ and $Y_3Ga_5O_{12}$), or only tetrahedral sites ($Li_{0.5}Ga_{2.5}O_4$ and $Y_3Ga_5O_{12}$), or both octahedral and tetrahedral sites (γ-Fe_2O_3), see details in Fig. 5. One can see that MCD in the range of 2.0 to 3.0 eV can be assigned to both the d-d transitions and pair transitions in Fe^{3+} ions. In particular, two overlapping intense MCD features can be ascribed to $^6A_{1g}(^6S) \rightarrow {}^4E_g, {}^4A_{1g}(^4G)$ and $2\ (^6A_{1g}) \rightarrow 2\ (^4T_{1g})$ transitions for Fe^{3+} in octahedral sites.

The observed changes of the MCD intensity on the Gd_2O_3 contents can be explained assuming that a part of Gd^{3+} ions is incorporated into ε-Fe_2O_3 nanoparticles, substituting Fe^{3+} ions, see above. As the ionic radius of Gd^{3+} is considerably larger than that of Fe^{3+}, respectively, 0.938 and 0.785 Å in octahedral sites [63], Gd^{3+} ions tend to occupy the most spacious iron sites in ε-Fe_2O_3 lattice. As seen in Table 1, the best candidate for accommodating Gd^{3+} is O1 site. It has been shown that the magnetic moments of trivalent rare earths, in particular of Gd^{3+} incorporated in different ferrites remain unordered [64,65]. Indeed, because of shielding of the partially filled 4f-shell by completely

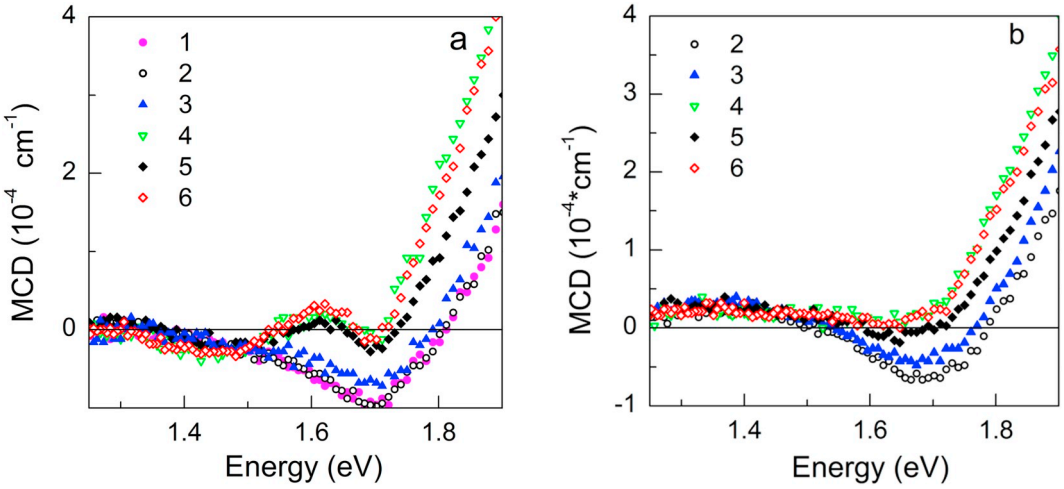

Fig. 7. MCD spectra for samples 1 to 6 at 295 (a) and 90 K (b) measured in the magnetizing field of 0.35 T. The curve numbers correspond to the sample numbers.

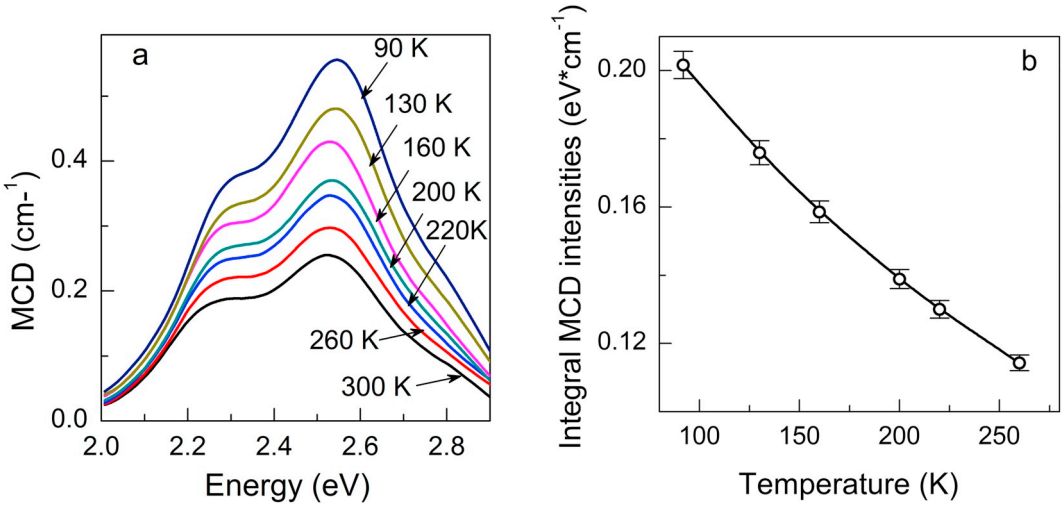

Fig. 8. MCD spectra for sample 2 measured at different temperatures in the magnetizing field of 0.35 T (a). Temperature dependence of the integral MCD intensity calculated as the area under the spectral curve in the range of 2.0 to 3.0 eV (b). The error bars show the accuracy of measurements.

Table 1
Fe—O distances (in nm) in different crystals. T, O, O1, O2 and O3 stand for tetrahedral and different octahedral sites, respectively.

Crystal, reference	Site	d_{Fe-O}	Average d_{Fe-O}
γ-Fe_2O_3 [61]	T	0.186, 0.188, 0.186, 0.192	0.188
	O	0.208, 0.208, 0.204, 0.204, 0.198, 0.198	0.203
$Y_3Fe_5O_{12}$ [62]	T	0.188	0.188
	O	0.200	0.200
ε-Fe_2O_3 [20]	T	0.184, 0.210, 0.184, 0.165	0.186
	O1	0.209, 0.213, 0.256, 0.191, 0.201, 0.192	0.210
	O2	0.203, 0.217, 0.184, 0.201, 0.194, 0.182	0.197
	O3	0.200, 0.200, 0.202, 0.212, 0.225, 0.185	0.204

filled 5 s- and 5p-shells [66,67], these ions do not experience exchange interaction with neighbouring iron ions. Therefore, substituting iron by gadolinium is expected to result in a decrease of the corresponding Fe^{3+} sublattice magnetization, so that the total magnetization of ε-Fe_2O_3, resulting from Fe^{3+} ions in O1 sites, decreases with the increase of Gd_2O_3 contents. As a consequence, the intensity of the MCD peaks due to electron transitions in Fe^{3+} ions in O1 sites also decreases. Besides, incorporating larger ions into the crystal lattice would distort neighbouring Fe^{3+} sites and therefore affect in different ways the intensities of MCD peaks related to different electron transitions.

As seen in Fig. 5, three electron transitions can contribute to the MCD spectrum in the range of 1.2 to 1.8 eV, viz.: $^6A_{1g}(^6S) \rightarrow {}^4T_{1g}$ (^4G), $^6A_{1g}(^6S) \rightarrow {}^4T_{2g}$ (^4G) for Fe^{3+} ions in O1 sites and $^6A_1$ (^6S) → $^4T_1$ (^4G) for Fe^{3+} ions in T sites. The energies of these transitions greatly depend on the crystal field strength, so that site-to-site distributions of the latter, caused by local disorder, result in broadening of the MCD peaks. A substitution of Fe^{3+} by Gd^{3+} in these sites should to a still greater extent affect MCD features related to these transitions. Indeed, noticeable changes of the MCD spectra in the lower energy range become obvious with the increase of Gd_2O_3 contents, see Fig. 7.

A more detailed study of the correspondence between the MCD features observed in this energy range and particular electron transitions is now in course.

3.4. Electron magnetic resonance

3.4.1. Experimental results

Fig. 9 shows EMR spectra at 120 and 300 K for sample 6. The spectra of all samples are quite similar, containing two conspicuous features with the effective g-factors $g = 4.3$ and 2.0. The third, much weaker low-field feature with $g = 6.0$ comes into view only at higher Gd_2O_3 contents.

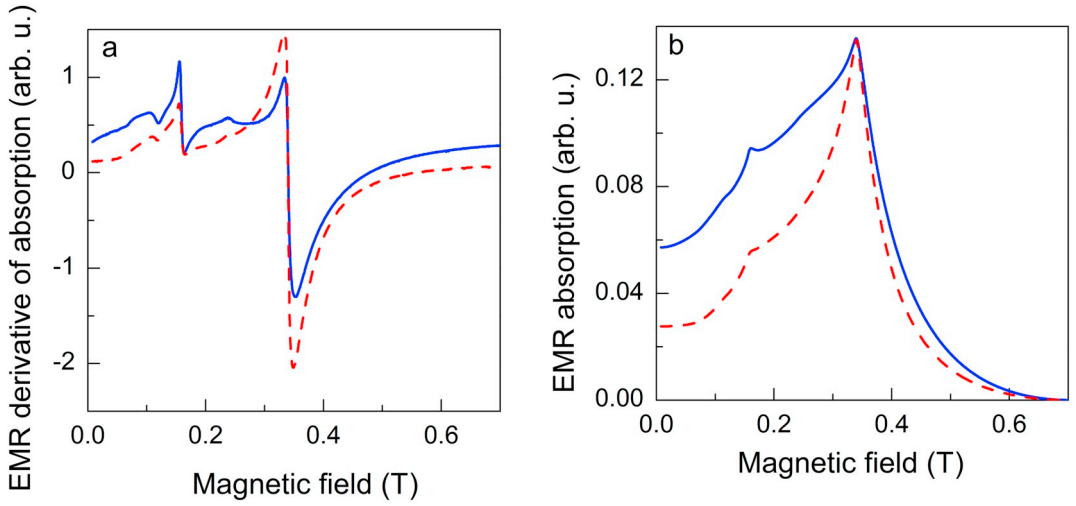

Fig. 9. EMR derivative-of-absorption (a) and absorption (b) spectra of sample 6 at 120 K (full line, blue online) and 300 K (dashed line, red online). (For interpretation of the references to colour in this figure legend, the reader is referred to the web version of this article.)

In the EMR spectra of iron- and gadolinium-containing borate glasses at least three distinct contributions are expected, viz., electron paramagnetic resonance (EPR) of paramagnetic Fe^{3+} and Gd^{3+} ions diluted in the glass matrix as well as EMR of magnetically ordered nanoparticles. The $g = 4.3$ feature is the signature of diluted Fe^{3+} ions in glass [68,69] while the $g = 6.0$ one is due to diluted Gd^{3+} ions [70], see also the computer simulations of EPR spectra of Fe^{3+} and Gd^{3+} ions described in detail in the following subsection.

The most intense EMR feature – that with $g = 2.0$ – a priori can be due to any of these species. Yet, for the $g = 2.0$ feature due to superparamagnetic nanoparticles, at lower temperatures, because of the blocking of their magnetic moments, one should expect a severe broadening as well as a spectacular downfield shift [69]. In the case of ε-Fe_2O_3 nanoparticles such a broadening has been reported earlier [23,24,41].

In the glasses studied in this work, a certain broadening of the $g = 2.0$ feature at lower temperatures is also observed; however, it is accompanied by a narrowing of the $g = 4.3$ one. Concomitantly, the relative intensity of the former feature decreases and that of the latter one increases, as seen in Fig. 9. These transformations are closely interrelated, implying that the $g = 2.0$ feature (at least, its predominant part) arises from the same paramagnetic species as the $g = 4.3$ one, i.e., from diluted Fe^{3+} ions. The above reasoning will be further corroborated by the computer simulations of Fe^{3+} EPR spectra, see below.

The possibility of attributing a significant part of the $g = 2.0$ feature to diluted Gd^{3+} ions can be ruled out; indeed, Fig. 10 shows a very sharp decrease of the ratio of amplitude of this feature in the EMR absorption spectra to Gd_2O_3 contents. Manifestly, most of Gd^{3+} ions do not contribute to this feature.

Fig. 11 shows EMR absorption intensities for different Gd_2O_3 contents at 120 and 300 K obtained by double integration over the magnetizing field of the derivative-of-absorption spectra. Clearly, the T^{-1} Ci law is not observed for these intensities; therefore, a significant contribution to the experimental spectra arises from non-diluted paramagnetic ions, supposedly contained in magnetic nanoparticles.

One can see that, at first glance, no distinct features attributable to EMR of nanoparticles are apparent in the experimental spectra. Indeed, the standard presentation of EMR spectra in the form of derivatives of absorption is unfavourable in the case where such particles are expected to occur, as far as it favours narrow spectral features at the expense of broader ones, whereas the magnetic nanoparticles usually give rise to more or less broad EMR features [71]. Therefore, in what follows we have chosen to deal with EMR *absorption* spectra obtained by integrating over the magnetizing field the corresponding derivative-of-

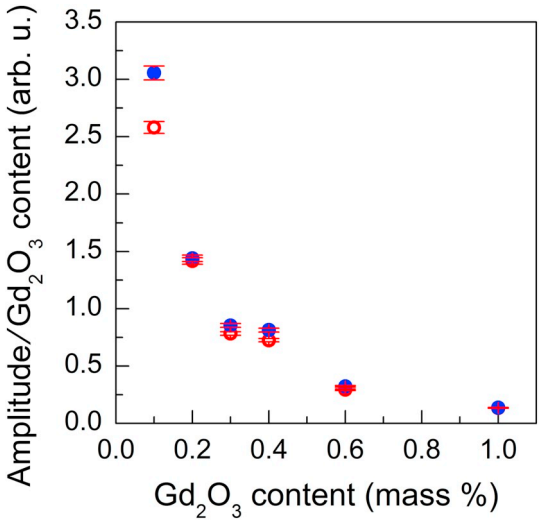

Fig. 10. Ratio of amplitudes of the $g = 2.0$ feature to Gd_2O_3 contents at 120 K (full circles, blue online) and 300 K (empty circles, red online) for different Gd_2O_3 contents. (For interpretation of the references to colour in this figure legend, the reader is referred to the web version of this article.)

absorption spectra. In Fig. 9 b we have plotted the EMR absorption spectra corresponding to the derivative-of-absorption spectra shown in Fig. 9 a; quite similar spectra have been obtained for all other samples.

3.4.2. *Computer simulations of the experimental EMR spectra*

In order to extract the absorption due to magnetic nanoparticles from the experimental EMR spectra, we have attempted to subtract from the latter spectra the contributions arising from paramagnetic ions diluted in the glass matrix. The corresponding EPR spectra have been calculated using the ab initio approach outlined by Le Caër et al. [72,73]. Although this approach has been put forward in order to describe nuclear magnetic resonance (NMR) spectra in disordered solids, mutatis mutandis it can be applied to EPR as well. Below we briefly outline its principal features in the latter case.

In the magnetic resonance spectroscopy (both NMR and EPR) the principal manifestation of local disorder is a distribution of relevant spectroscopic parameters. The EPR of Fe^{3+} and Gd^{3+} in glasses can be adequately described by the following spin Hamiltonian, containing only the Zeeman and “quadrupole” fine structure (qfs) terms [69]:

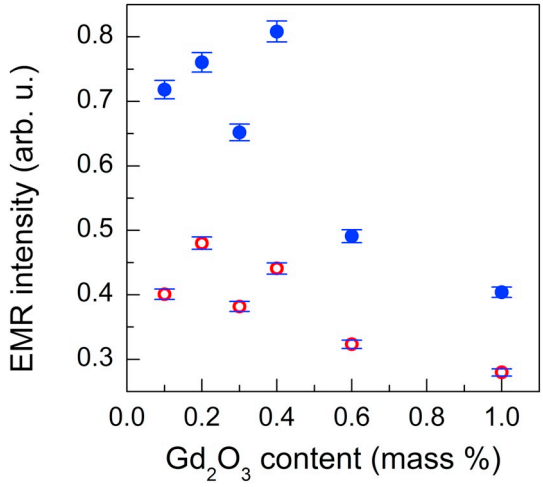

Fig. 11. Integral EMR intensities for different Gd_2O_3 contents at 120 K (full circles, blue online) and 300 K (empty circles, red online). (For interpretation of the references to colour in this figure legend, the reader is referred to the web version of this article.)

$$\mathscr{H} = g\beta \boldsymbol{B}\cdot\boldsymbol{S} + \sum_{i=-2}^{2} B_2^i O_2^i \tag{2}$$

where g for S-ions is very close to the free-electron g-value $g_e = 2.0023$, $O_2{}^i$ are extended Stevens operators and $B_2{}^i$ are the corresponding qfs parameters. The assembly of the latter parameters can be represented as a sum of two traceless tensors $\boldsymbol{D}_0 + \boldsymbol{D}$ with components symmetric with respect to their main diagonals. $\boldsymbol{D}_0$ is a fixed tensor characterizing a paramagnetic ion in a perfect crystal. In the coordinate frame where it is diagonal,

$$\boldsymbol{D}_0 = \begin{pmatrix} E_0 - \frac{1}{3}D_0 & 0 & 0 \\ 0 & -E_0 - \frac{1}{3}D_0 & 0 \\ 0 & 0 & \frac{2}{3}D_0 \end{pmatrix} \tag{3}$$

Here D_0 and E_0 are, respectively, the "axial" and "rhombic" qfs parameters in the absence of disorder. In choosing the principal axes of $\boldsymbol{D}_0$, the convention $0 \le \frac{E_0}{D_0} \le \frac{1}{3}$ is usually applied. In turn, $\boldsymbol{D}$ is a random tensor with statistically distributed components; in order to satisfy the requirements of diagonal symmetry and tracelessness as well as of rotational invariance, these components are expressed as linear combinations of five normally distributed random quantities U_i, $i = 1, \ldots, 5$ with zero mean values and equal standard deviations $\frac{1}{2}\sigma$ where σ is the standard deviation of the D_{zz} component [73]:

$$\boldsymbol{D} = \sqrt{3}\begin{pmatrix} -\frac{1}{\sqrt{3}}U_1 + U_5 & U_4 & U_2 \\ U_4 & -\frac{1}{\sqrt{3}}U_1 - U_5 & U_3 \\ U_2 & U_3 & \frac{2}{\sqrt{3}}U_1 \end{pmatrix} \tag{4}$$

We have put forward a simulation code implementing the above model. For a given set of adjustable parameters E_o, D_0 and σ, this code

i. generates the random quantities U_i, $i = 1, 2, \ldots, 5$;

ii. using Eqs. (2) to (4) computes and diagonalizes the $\boldsymbol{D}_0 + \boldsymbol{D}$ tensor;
iii. calculates the EPR absorption and derivative-of-absorption spectra.

Preliminary simulations have shown that in the actual case D_0 and E_0 are negligible compared to σ. Note that in this case there exists an analytical form of the joint distribution density of qfs parameters, the so-called Czjzek's function [74,75]. The latter has been used, in particular, by Legein et al. for simulating EPR spectra of transition ions in fluoride glasses.

Fig. 12 illustrates the transformation with σ of computer-generated EPR *absorption* spectra of Fe^{3+} and Gd^{3+} ions. At low σ-values, for both ions only the $g = 2.0$ feature is observed, as expected for sites with relatively small qfs parameters [68–70]. With the increase of σ-value these features broaden and finally vanish. Concurrently, in the case of Fe^{3+}, the $g = 4.3$ feature forms, characteristic of this ion in strongly disordered sites [68,69], and gradually narrows as σ increases. In the case of Gd^{3+}, for intermediate σ-values the feature with $g = 6.0$ occurs, arising from inter-Kramers-doublet transitions in a certain range of the

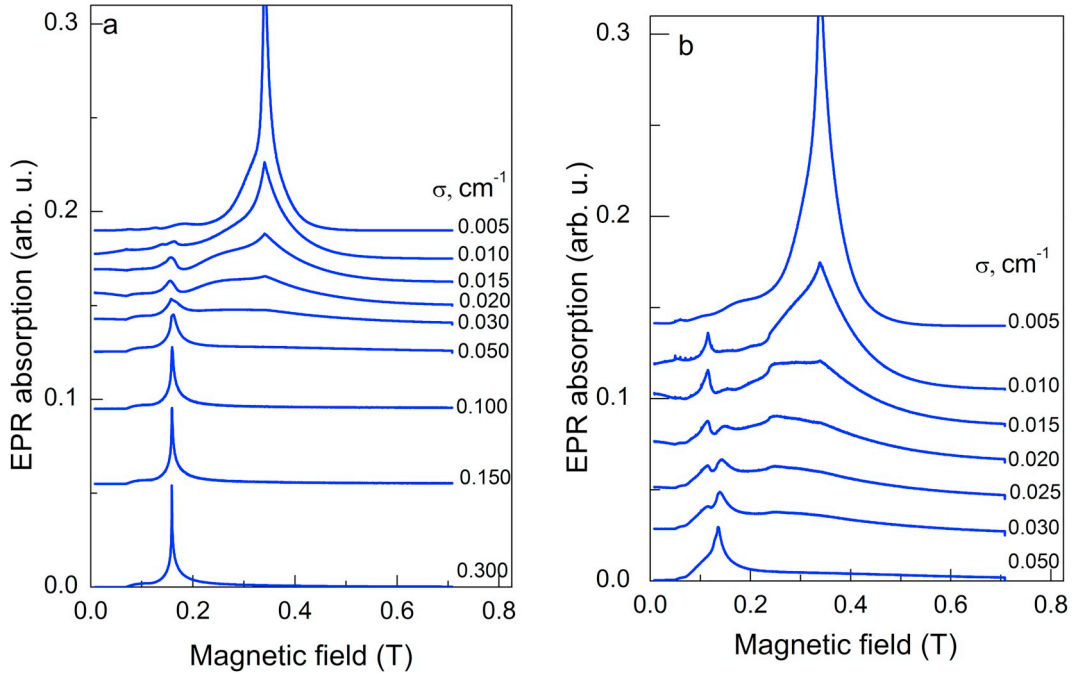

Fig. 12. Computer-generated X band EPR absorption spectra of Fe^{3+} (a) and Gd^{3+} ions (b) for $D_0 = 0$ and $E_0 = 0$, and different σ-values shown alongside the curves.

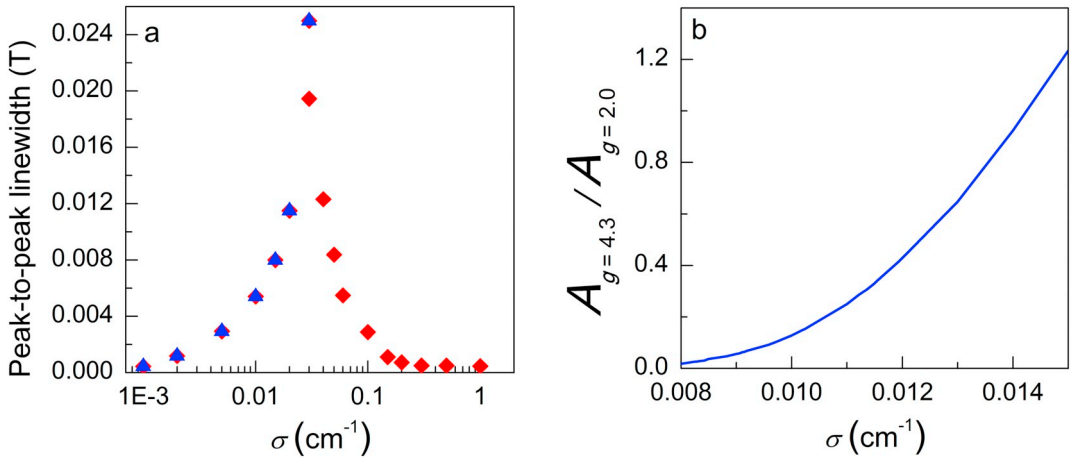

Fig. 13. Theoretical peak-to-peak linewidths of Fe^{3+} $g = 4.3$ (diamonds, red online) and $g = 2.0$ (triangles, blue online) derivative-of-absorption features calculated for different σ-values (a). Ratio of amplitudes of these features (b). (For interpretation of the references to colour in this figure legend, the reader is referred to the web version of this article.)

qfs parameters [68,69], and for larger σ only a feature with $g = 5.0$ is observed, arising from one of the central Kramers doublets [70]. Note that latter feature is not observable in the experimental spectra, cf. Figs. 9 and 12.

At this stage, we can subtract from the experimental EMR absorption spectra the computer-generated EPR absorption spectra of Fe^{3+} ions. However, cf. Fig. 12, the latter spectra are highly sensitive to the σ-values determining the qfs parameters in Eq. (2), and these parameters can be not only structure- but also temperature-dependent, e.g., see Daubric et al. [76] and references quoted therein. Therefore, implementing the subtraction procedure is somewhat arduous; indeed, for each glass sample and at each temperature a particular σ-value should be selected for calculating the appropriate Fe^{3+} EPR spectrum.

Fig. 13 a shows the peak-to-peak widths of the derivative-of-absorption features with $g = 4.3$ and 2.0 and the ratio of their amplitudes in the computer-generated Fe^{3+} EPR spectra. As one can see, both features are simultaneously observable only in a relatively narrow range of σ-values. Thus, the relevant σ-value in each case has been determined by comparing the peak-to-peak linewidths of the $g = 4.3$ and 2.0 features in the experimental derivative-of-absorption spectra with Fig. 13 a and further pinpointed by comparing the ratio of the corresponding amplitudes with the curve in Fig. 13 b. The results of applying this procedure are illustrated in Fig. 14 for sample 6 at 120 and 300 K.

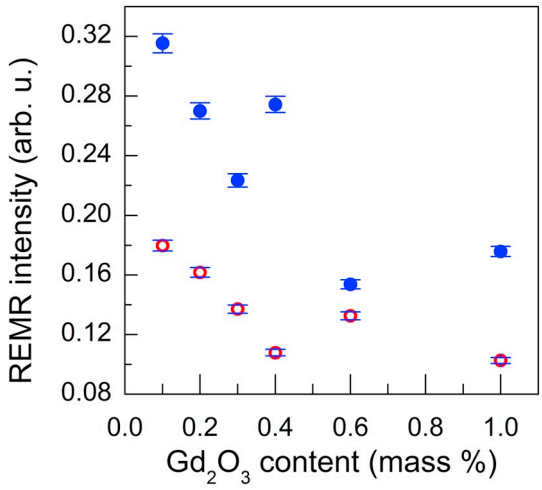

Fig. 15. REMR absorption intensities at different Gd_2O_3 contents at 120 K (full circles, blue online) and 300 K (empty circles, red online). (For interpretation of the references to colour in this figure legend, the reader is referred to the web version of this article.)

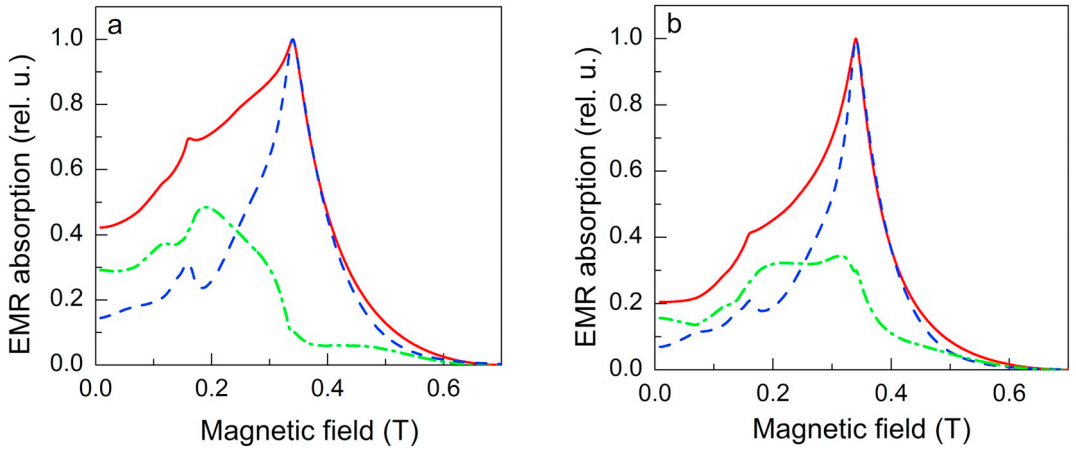

Fig. 14. Extracting the absorption due to EMR of nanoparticles and EPR of diluted Gd^{3+} ions from the experimental EMR spectra of sample 6 (a, 120 K, b, 300 K). Full lines (red online): experimental spectra, dashed lines (blue online): computer-generated EPR spectra of diluted Fe^{3+} ions and dash-dotted lines (green online): remaining EMR (REMR) spectra. (For interpretation of the references to colour in this figure legend, the reader is referred to the web version of this article.)

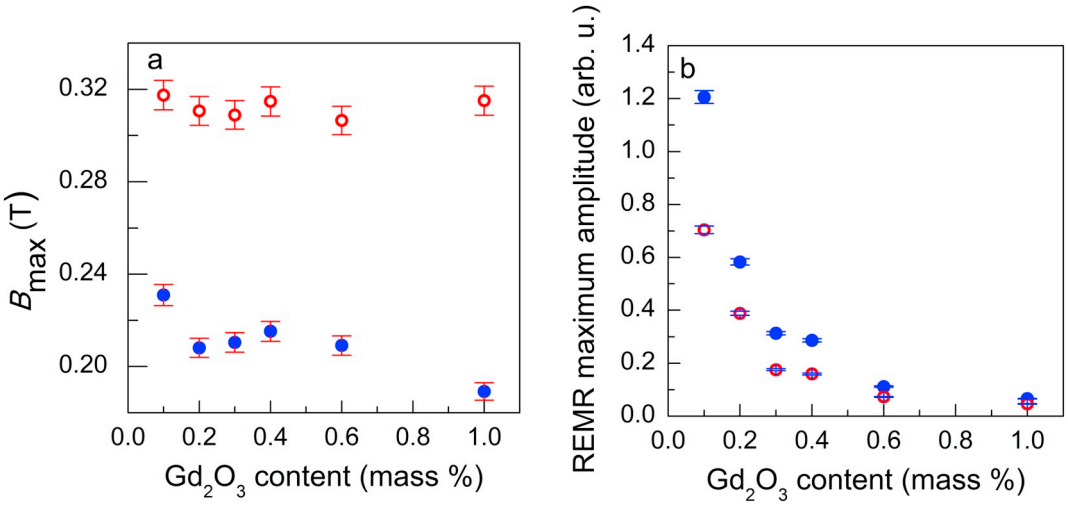

Fig. 16. Positions of the REMR absorption maxima at different Gd_2O_3 contents (a) and amplitudes of these maxima (b) at 120 K (full circles, blue online) and 300 K (empty circles, red online). (For interpretation of the references to colour in this figure legend, the reader is referred to the web version of this article.)

Fig.15 shows the *remaining* EMR (REMR) absorption intensities in glasses with different Gd_2O_3 contents at 120 and 300 K. Note that the decrease in the REMR intensity with the increase in Gd_2O_3 contents correlates well with the corresponding decrease of the MCD intensity, cf. Fig. 6.

A priori, the REMR spectra can contain contributions of both EMR of magnetic nanoparticles and of EPR of diluted Gd^{3+} ions. Fig. 16 a shows the positions of the REMR absorption maxima in samples 1 to 6 at 120 and 300 K. As one can see, cf. Fig. 12 b, these maxima occur in the magnetizing field range where absorption maxima for Gd^{3+} are expected to occur only for σ-values in the range between 0.015 and 0.025 cm^{-1}. Yet, as clearly seen in the same figure; in this range the Gd^{3+} feature with $g = 5.0$ should also be present, which is not the case in the experimental EMR spectra. Moreover, the amplitudes of these maxima do *not* increase with Gd_2O_3 contents in the glasses, see Fig. 16 b. Finally, with decreasing the temperature these maxima shift downfield, as expected for the superparamagnetic resonance spectra [71]. On the basis of this reasoning, the REMR maxima can be ascribed to the EMR of magnetic nanoparticles. The fact that such shift has not been observed in earlier studies of ε-Fe_2O_3 nanoparticles [23,24,41,71] can be due to dissimilarity in morphological characteristics of the nanoparticles as well in the nature and structure of their shell. Indeed, the latter is expected to be significantly different for nanoparticles supported on silica (as those described in the above-quoted studies) or those formed in the borate glass matrix (as in the present case).

4. Role of gadolinium in the formation of nanoparticles in borate glasses

The analysis of results described above allows to conclude that the characteristics of the magnetic nanoparticles arising in aluminoborate glasses modified with K_2O and doped with Fe_2O_3 and Gd_2O_3 significantly differ from those of γ-Fe_2O_3 nanoparticles in previously described glasses containing one more glass-forming oxide – GeO_2 – and doped with Fe_2O_3 and different rare earth oxides including Gd_2O_3 [19,51]. A number of properties of the nanoparticles in the glasses studied in this work are similar to those of ε-Fe_2O_3 nanoparticles earlier described in the literature, see Introduction, viz., the reflections (133) and (335) in XRD patterns characteristic of ε-Fe_2O_3, strong magnetization and MCD increase with the decrease of temperature and higher coercivity in comparison with γ-Fe_2O_3 nanoparticles mentioned above [19]. On the other hand, their coercivity is noticeably lower than that observed in most samples containing ε-Fe_2O_3 nanoparticles [36,37]. However, room-temperature coercivity of very fine, ca. 3 nm, ε-Fe_2O_3 nanoparticles turns out to be rather low, ca. 0.1 T, and does not significantly change with decreasing the temperature [41]. Besides, in this case peculiarities in the temperature dependences of remnant magnetization and coercivity, usually observed for ε-Fe_2O_3 nanoparticles near 100 K, e.g., see Gish et al. [22], were absent. Balaev et al. [23] have ascribed these discrepancies to an increased surface contribution to the total magnetic anisotropy of ε-Fe_2O_3 fine particles (responsible for the peculiarities in the nanoparticle magnetic characteristics). However, the differences of nanoparticle magnetic characteristics in iron- and gadolinium-containing borate glasses from those usually observed for ε-Fe_2O_3 nanoparticles is rather due to the incorporation of significant amounts of Gd^{3+} ions in the nanoparticle lattice altering their magnetic anisotropy.

Several authors have shown that the presence of gadolinium favours phase separation in borate glasses [77,78]. Hence, doping with Gd_2O_3 is expected to provide favourable conditions for the formation of nanoparticles in the glass. Indeed, in sample 1 containing 0.1 mass % of Gd_2O_3 only fine and sparse nanoparticles are present, see Fig. 1, and for this sample minimum MCD intensity is observed, see Fig. 6. On the other hand, the ratio of amplitudes of the $g = 2.0$ EMR feature to Gd_2O_3 contents is maximum for this sample, cf. Fig. 13. This can be explained by the fact that this feature predominantly arises from Fe^{3+} ions diluted in the glass matrix while MCD is mainly due to these ions incorporated into magnetically ordered nanoparticles. Low solubility of Gd_2O_3 in glasses, in particular, in borate glasses has been shown using different experimental techniques [77,79,80]. For instance, for gadolinium-containing borosilicate glasses the following model of Gd^{3+} partitioning was suggested: firstly, Gd^{3+} ions substitute B^{3+} in very low quantity; then Gd^{3+} begins substituting Si^{3+}, and finally Gd^{3+} ions aggregate, so that their crystallization can occur [77]. Such behaviour is usually observed for Gd_2O_3 contents lower than 1% [77–79,81]. Thus, the hypothesis that in iron- and gadolinium-containing glasses the main part of Gd^{3+} ions are incorporated in the nanoparticles, substituting Fe^{3+} ions in the most "spacious" O1 sites, see Section 3.3, seems quite reasonable. Indeed, this is clearly seen for sample 6 with the highest (1.0 mass %) Gd_2O_3 content, see Fig. 2. The concomitant decrease of Fe^{3+} concentration in these sites (giving the main contribution to magnetization and hence to MCD) is expected to manifest itself in a decrease of nanoparticle magnetization with the increase of Gd_2O_3 contents, as indeed has been observed in the present study.

One can see that in iron- and gadolinium-containing glasses gadolinium has a dual role. On the one hand, an increase of Gd_2O_3 content favours the formation of nanoparticles and on the other hand, it reduces the nanoparticle magnetization. In determining the magnetic

characteristics such glasses, the first and the second trends prevail at lower and at higher Gd_2O_3 contents, respectively.

5. Conclusions

In borate glasses of composition 22.5 K_2O-22.5 Al_2O_3–55 B_2O_3 doped with low content of Fe_2O_3 (1.5 mass %) and co-doped with various contents of Gd_2O_3 (from 0.1 to 1.0 mass %) magnetically ordered nanoparticles have been shown to arise after additional thermal treatment.

The analysis of the set of experimental results, namely, of certain structural characteristics of the nanoparticles, in particular, of interplanar distances in the nanoparticle lattice and positions of XRD reflections, as well as of static magnetic properties and MCD temperature dependences, allows identifying the predominant magnetic phase in the glasses as ε-Fe_2O_3. At that, considerable part of iron ions is shown to be substituted by gadolinium, and the degree of substitution of iron by gadolinium depends on Gd_2O_3 contents in the charge.

The non-monotonic variation of the MCD intensity with Gd_2O_3 content suggests that gadolinium plays a dual role in determining the magnetic characteristics of the glasses, on the one hand, favouring the formation of nanoparticles and on the other hand, reducing their magnetization by substituting iron in the nanoparticle lattice. From the point of view of MCD characteristics, the optimal doping level is about 0.2% of Gd_2O_3.

Significant correlations have been found between the variations of intensities of MCD and EMR with the increase of Gd_2O_3 contents. Computer analysis and simulation of the EMR spectra of the glasses allow separating the contributions of the diluted iron ions and of the nanoparticles; besides, they demonstrate a superparamagnetic behaviour of the nanoparticles in accordance with the temperature dependences of the nanoparticle magnetization characteristic for an ensemble of superparamagnetic nanoparticles.

Acknowledgments

The work is supported by Russian Academy of Sciences in the frame of the Project № 0356-2017-0030.

References

[1] Y.-K. Lee, S.-Y. Choi, Controlled nucleation and crystallization in Fe_2O_3-CaO-SiO_2 glass, J. Mater. Sci. 32 (1997) 431–436.
[2] M. Hayashi, M. Susa, K. Nagata, Magnetic interaction between magnetite particles dispersed in calcium-silicate glasses, J. Magn. Magn. Mater. 171 (1997) 170–178.
[3] N. Rezlescu, L. Rezlescu, Irreversible structural changes by heat treatments within the amorphous matrix Fe_2O_3-Li_2O-B_2O_3, Mater. Sci, Engineering 375-377 (2004) 1273–1276.
[4] D.D. Zaytsev, P.E. Kazin, A.V. Garshev, Y.D. Tret'yakov, M. Jansen, Synthesis and magnetic properties of SrO-Fe_2O_3-B_2O_3 glass-ceramics, Inorg. Mater. 40 (2004) 881–885.
[5] S. Woltz, R. Hiergeist, P. Gornert, C. Russel, Magnetite nanoparticles prepared by the glass crystallization method and their physical properties, J. Magn. Magn. Mater. 298 (2006) 7–13.
[6] K. Sharma, S. Singh, C.L. Prajapat, S. Bhattacharya, M.R. Singh Jagannath, S.M. Yusuf, G.P. Kothiyal, Preparation and study of magnetic properties of silico phosphate glass and glass-ceramics having iron and zinc oxide, J. Magn. Magn. Mater. 321 (2009) 3821–3828.
[7] S. Amlah, M. Azmi, M.R. Sahar, Optical response and magnetic characteristic of samarium doped zinc phosphate glasses containing nickel nanoparticles, J. Magn. Magn. Mater. 393 (2015) 341–346.
[8] K. Sharma, A. Dixit, S. Singh, S. Bhattacharya Jagannath, C.L. Prajapat, P.K. Sharma, S.M. Yusuf, A.K. Tyagi, G.P. Kothiyal, Preparation and studies on surface modifications of calcium-silico-phosphate ferrimagnetic glass-ceramics in simulated body fluid, Mater. Sci. Eng. C29 (2009) 2226–2233.
[9] H. Akamatsu, K. Tanaka, K. Fujita, S. Murai, Magnetic phase transitions in Fe_2O_3-Bi_2O_3-B_2O_3 glasses, J. Phys. Condens. Matter 20 (9) (2008) 235216.
[10] H. Akamatsu, K. Fujita, S. Murai, K. Tanaka, Magneto-optical properties of transparent divalent iron phosphate glasses, Appl. Phys. Lett. 92 (2008) 251908.
[11] M.S. Dahiya, A. Yadav, N. Manyani, S. Chahal, A. Hooda, A. Agarwal, S. Khasa, Fe-substituted Co-Li bismuth borate glasses. Crystallization kinetics and optical absorption, J. Therm. Anal. Calorim. 126 (2016) 1191–1199.
[12] A. Karamanov, M. Pelino, Crystallization phenomena in iron-rich glasses, J. Non-Cryst. Solids 281 (2001) 139–151.
[13] V. Sandu, S. Greculeasa, A. Kuncser, M.S. Nicolescu, V. Kuncser, Effect of Cr_2O_3 on the magnetic properties of magnetite-based glass-ceramics obtained by controlled crystallization of Fe-containing aluminoborosilicate glass, J. Eur. Ceram. Soc. 37 (2017) 3089–3099.
[14] V. Sandu, E. Cimpoiasu, S. Greculeasa, A. Kuncser, M.S. Nicolescu, V. Kuncser, Magnetite-based glass-ceramics prepared by controlled crystallization of relaxation, Ceram. Int. 43 (2017) 3405–3413.
[15] J. Liu, M. Zhang, C. Zhu, S. Liu, Y. Zhang, Preparation and properties of ferromagnetic glass-ceramics and glass fibers in alkali-free and high-iron glass system, Ceram. Int. 43 (2017) 4295–4301.
[16] M. Georgieva, D. Tzankov, R. Harizanova, G. Avdeev, C. Russel, Magnetic properties of magnetite nanoparticles crystallized in sodium-aluminoborosilicate glass matrix, Appl. Phys. A Mater. Sci. Process. 122 (2016) 160 (7 pages).
[17] A. Hoell, A. Wiedenmann, U. Lembke, R. Kranold, The non-magnetic surface of magnetic particles in nanostructured glass ceramics studied by SANS, Physica B 276–278 (2000) 886–887.
[18] W. Wisniewski, R. Harizanova, G. Volkscha, C. Russel, Crystallization of iron containing glass–ceramics and the transformation of hematite to magnetite, Cryst. Eng. Comm. 13 (2011) 4025–4031.
[19] I.S. Edelman, O.S. Ivanova, E.A. Petrakovskaja, D.A. Velikanov, I.A. Tarasov, Y.V. Zubavichus, N.N. Trofimova, V.I. Zaikovskii, Formation, characterization and magnetic properties of maghemite γ-Fe_2O_3 nanoparticles in borate glasses, J. Alloys Compd. 624 (2015) 60–67.
[20] J. Tucek, R. Zboril, A. Namai, S. Ohkoshi, ε-Fe_2O_3: an advanced nanomaterial exhibiting giant coercive field, millimeter-wave ferromagnetic resonance, and magnetoelectric coupling, Chem. Mater. 22 (2010) 6483–6505.
[21] E. Tronc, C. Chanéac, J.P. Jolivet, Structural and magnetic characterization of ε-Fe_2O_3, J. Solid St. Chem. 139 (1998) 93–104.
[22] M. Gich, A. Roig, C. Frontera, E. Molins, J. Sort, M. Popovici, G. Chouteau, D.M. Marero, J. Nogues, Large coercivity and low-temperature magnetic reorientation in ε-Fe_2O_3 nanoparticles, J. Appl. Phys. 98 (2005) 044307.
[23] D.A. Balaev, A.A. Dubrovskiy, K.A. Shaykhutdinov, O.A. Bayukov, S.S. Yakushkin, G. Bukhtiyarova, O.N. Martyanov, Surface effects and magnetic ordering in few-nanometre-sized ε-Fe_2O_3 particles, J. Appl. Phys. 114 (2013) 163911.
[24] S.S. Yakushkin, G.A. Bukhtiyarova, O.N. Martyanov, Formation conditions of a magnetically ordered phase ε-Fe_2O_3. AFMR in-situ study, J. Struct. Chem. 54 (2013) 876–882.
[25] D.A. Balaev, I.S. Poperechny, A.A. Krasikov, K.A. Shaikhutdinov, A.A. Dubrovskiy, S.I. Popkov, A.D. Balaev, S.S. Yakushkin, G.A. Bukhtiyarova, O.N. Martyanov, Yu.L. Raikher, Dynamic magnetization of ε-Fe_2O_3 in pulse field: evidence of surface effect, J. Appl. Phys. 117 (2015) 063908.
[26] M. Kovacheva, O. Rodrıguez de la Fuente, Epsilon iron oxide: Origin of the high coercivity stable low Curie temperature magnetic phase found in heated archeological materials, Geochem. Geophys. Geosyst. 18 (2017) 2646–2656.
[27] A. Sivkov, E. Naiden, A. Ivashutenko, I. Shanenkov, Plasma dynamic synthesis and obtaining ultrafine powders of iron oxides with high content of ε-Fe_2O_3, J. Magn. Magn. Mater. 405 (2016) 158–168.
[28] R. Zboril, M. Mashlan, D. Petridis, Iron(III) oxides from thermal processes, synthesis, structural and magnetic properties, Moessbauer spectroscopy characterization and applications, Chem. Mater. 14 (2002) 969–982.
[29] R. Schrader, G. Buttner, Eine neue Eisen(III)-oxidphase: ε-Fe_2O_3, Z. Anorg. Allg. Chem. 320 (1963) 220–234.
[30] I. Dezsi, J.M.D. Coey, Magnetic and thermal properties of ε-Fe_2O_3, Phys. Stat. Solidi. A 15 (1973) 681–685.
[31] S.C. Abrahams, J.M. Reddy, J.L. Bernstein, Crystal structure of piezoelectric ferromagnetic gallium iron oxide, J. Chem. Phys. 42 (1965) 3957–3968.
[32] F. Bouree, J.L. Badour, E. Elabraoui, J. Musso, C. Laurent, A. Rousset, Crystal and magnetic structure of piezoelectric, ferrimagnetic and magnetoelectric aluminium iron oxide $FeAlO_3$ from neutron powder diffraction, Acta Crystallogr., Sect. B 52 (1996) 217–222.
[33] L. Smrčok, L.V. Langer, M. Halvarsson, S.Z. Ruppi, A new Rietveld refinement of k-Al_2O_3, Kristallografiya 216 (2001) 409–412.
[34] K. Kelm, W. Mader, Synthesis and structural analysis of ε-Fe_2O_3, Z. Anorg. Allg. Chem. 631 (2005) 2383–2389.
[35] J. Kohout, P. Brazda, K. Zaveta, D. Kubaniova, T. Kmjec, L. Kubıckova, M. Klementova, E. Santava, A. Lancok, The magnetic transition in ε-Fe_2O_3 nanoparticles: magnetic properties and hyperfine interactions from Mössbauer spectroscopy, J. Appl. Phys. 117 (2015) 17D505.
[36] J. Jian, S.-I. Oshkoshi, K. Hashimoto, Giant coercive field of nanometer-sized iron oxide, Adv. Mater. 16 (2004) 48–51.
[37] M. Gich, C. Frontera, A. Roig, E. Taboada, E. Molins, H.R. Rechenberg, J.D. Ardisson, W.A.A. Macedo, C. Ritter, V. Hardy, J. Sort, V. Skumryev, J. Nogues, High- and low-temperature crystal and magnetic structures of ε-Fe_2O_3 and their correlation to its magnetic properties, Chem. Mater. 18 (2006) 3889–3897.
[38] M. Popovici, M. Gich, D. Niznansky, A. Roig, C. Savii, L. Casas, E. Molins, K. Zaveta, C. Enache, J. Sort, S. de Brion, G. Chouteau, J. Nogues, Optimized synthesis of the elusive ε-Fe_2O_3 phase via sol-gel chemistry, Chem. Mater. 16 (2004) 5542–5548.
[39] V.N. Nikolić, M. Tadic, M. Panjan, L. Kopanjac, N. Cvjeticanin, V. Spasojevic, Influence of annealing treatment on magnetic properties of Fe_2O_3/SiO_2 and formation of ε-Fe_2O_3 phase, Ceram. Int. 43 (2017) 3147–3155.
[40] K.C. Barick, B.S.D.Ch.S. Varaprasad, D. Bahadur, Structural and magnetic properties of γ- and ε-Fe_2O_3 nanoparticles dispersed in silica matrix, J. Non-Cryst. Solids 356 (2010) 153–159.
[41] A.A. Dubrovskiy, D.A. Balaev, K.A. Shaykhutdinov, O.A. Bayukov, O.N. Pletnev, S.S. Yakushkin, G.A. Bukhtiyarova, O.N. Martyanov, Size effects in the magnetic

properties of ε- Fe_2O_3 nanoparticles, J. Appl. Phys. 118 (2015) 213901.
[42] J. López-Sánchez, A. Muñoz-Noval, C. Castellano, A. Serrano, A. del Campo, M. Cabero, M. Varela, M. Abuín, J. de la Figuera, J.F. Marco, G.R. Castro, O. Rodríguez de la Puente, N. Carmona, Origin of the magnetic transition at 100 K in epsilon-Fe_2O_3 nanoparticles studied by X-ray absorption fine structure spectroscopy, J. Phys. Condens. Matter 29 (48) (2017) 11 485701.
[43] O.S. Ivanova, R.D. Ivantsov, I.S. Edelman, E.A. Petrakovskaja, D.A. Velikanov, Y.V. Zubavichus, V.I. Zaikovskii, S.A. Stepanov, Identification of ε-Fe_2O_3 nanophase in borate glasses doped with Fe and Gd, J. Magn. Magn. Mater. 401 (2016) 880–889.
[44] O.S. Ivanova, R.D. Ivantsov, I.S. Edelman, E.A. Petrakovskaja, A comparative study of γ-Fe2O3 and ε-Fe_2O_3 nanoparticles arising in borate glasses doped with Fe and Gd, J. Siberian Fed. Univ. Math. Phys. 9 (2016) 459–462.
[45] O. Ivanova, J. Kliava, I. Edelman, R. Ivantsov, E. Petrakovskaja, Microwave and magneto-optic properties of ε-Fe_2O_3 arising in borate glasses doped with Fe and Gd, EPJ Web Confer. 185 (2018) 03011.
[46] I. Edelman, J. Kliava, Oxide glasses with magnetic nanoparticles: transparent magnets (Faraday rotation and electron magnetic resonance studies, feature article), Phys. Status Solidi B 246 (2009) 2197–2201.
[47] L. Walter-Levy, E. Quémeneur, On the hydrolysis of ferric sulphate at 100°C, C.R. Acad. Sci. 257 (1963) 3410–3413.
[48] S. Chakrabarty, K. Chatterjee, Oriented growth of α-Fe2O3 nanocrystals with different morphology. And their optical behavior, J. Cryst. Growth 381 (2013) 107–113.
[49] A. Demortiere, P. Panissod, B.P. Pichon, G. Pourroy, D. Guillon, B. Donnio, S. Begin-Colin, Size-dependent properties of magnetic iron oxide nanocrystals, Nanoscale 3 (2011) 225–232.
[50] H. Yao, Y. Ishikawa, Finite size effect on magneto-optical responses of chemically modified Fe_3O_4 nanoparticles studied by MCD spectroscopy, J. Phys. Chem. C 119 (2015) 13224–13230.
[51] I. Edelman, O. Ivanova, R. Ivantsov, E. Petrakovskaja, D. Velikanov, V. Zabluda, L. Hennet, D. Thiaudière, M.-L. Saboungi, Y. Zubavichus, S. Stepanov, V. Zaikovskii, A. Artemenko, J. Kliava, Nanoparticle-containing glasses co-doped with transition and rare earth elements: comparative studies of transparent magnets, Phys. Chem. Glasses Eur. J. Glass Sci. Technol. B 53 (2) (2012) 37–44.
[52] S.V. Vonsovsky, Magnetism, Wiley, 1974 (in two volumes).
[53] A.K. Singh, O.N. Srivastava, K. Singh, Shape and size-dependent magnetic properties of Fe_3O_4 nanoparticles synthesized using piperidine, Nanoscale Res. Lett. 12 (2017) 298.
[54] M. Lenglet, F. Hochu, Z. Šimša, Covalency of Fe^{3+}–O^{2+} bonds and magnetic structure in mixed oxides, Mater. Res. Bull. 33 (1998) 1821–1833.
[55] J.J. Krebs, W.G. Maisch, Exchange effects in the optical absorption spectrum of Fe^{3+} in Al_2O_3, Phys. Rev. B 4 (1971) 757–769.
[56] F. Varsanyi, G.H. Dieke, Ion-pair resonance mechanism of energy transfer in rare earth crystal fluorescence, Phys. Rev. Lett. 7 (1961) 442–444.
[57] J. Ferguson, H.J. Guggenheim, Y. Tanabe, Simultaneous electronic excitation of exchange-coupled pairs of manganese and nickel ions, Phys. Rev. 161 (1967) 207–211.
[58] D.M. Sherman, T.D. Waite, Electronic spectra of Fe^{3+} oxides and oxide hydroxides in the near IR to near UV, Am. Mineral. 70 (1985) 1262–1269.
[59] M. Pardavi-Horvath, I. Foldvari, I. Fellegvar, L. Gosztonyi, J. Paitz, Spectroscopic properties of Ca^{2+}-doped GGG, Phys. Status Solidi A 84 (1984) 547–553.
[60] Y. Tanabe, S. Sugano, On the absorption spectra of complex ions II, J. Phys. Soc. Jpn. 9 (1954) 766–779.
[61] C. Greaves, A powder neutron investigation of vacancy ordering and covalence in γ-Fe_2O_3, J. Sol. St. Chem. 49 (1983) 325–333.
[62] S. Geller, M.A. Gilleo, The crystal structure and ferrimagnetism of yttrium–iron garnet $Y_3Fe_2(FeO_4)_3$, Phys, Chem. Sol. 3 (1957) 30–36.
[63] R.D. Shannon, Revised effective ionic radii and systematic studies of interatomic distances in halides and chalcogenides, Acta Cryst A32 (1976) 751–767.
[64] O.M. Hemeda, M.Z. Said, M.M. Barakat, Spectral and transport phenomena in Ni ferrite-substituted Gd_2O_3, J. Magn. Magn. Mater. 224 (2001) 132–142.
[65] J. Jing, L. Liangchao, X. Feng, Structural analysis and magnetic properties of Gd-doped Li-Ni ferrites prepared using rheological phase reaction method, J. Rare Earths 25 (2007) 79–83.
[66] Ch. Kittel, Introduction to Solid State Physics, 7th ed., Wiley, 1995.
[67] B. Johansson, A. Rosengren, Generalized phase diagram for the rare earth elements: calculations and correlations of bulk properties, Phys. Rev. B 11 (1975) 2836–2857.
[68] R. Aasa, Powder line shapes in the electron paramagnetic resonance spectra of high-spin ferric complexes, J. Chem. Phys. 52 (1970) 3919–3930.
[69] J. Kliava, R. Berger, Magnetic resonance spectroscopy of iron-doped glasses: From isolated ions to clusters and nanoparticles, Recent Res. Devel. Non-Crystalline Solids, 3 Transworld Research Network, 2003, pp. 41–84 ISBN 81–7895–090-1.
[70] C.M. Brodbeck, L.E. Iton, The EPR spectra of Gd^{3+} and Eu^{2+} in glassy systems, J. Chem. Phys. 83 (1985) 4285–4299.
[71] J. Kliava, EMR of nanoparticles: superparamagnetic resonance, in: S. Gubin (Ed.), Magnetic Nanoparticles, Wiley-VCH, 2009, pp. 255–302.
[72] G. Le Caër, R.A. Brand, General models for the distributions of electric eld gradients in disordered solids, J. Phys. Condens. Matter 10 (1998) 10715–10774.
[73] G. Le Caër, B. Bureau, D. Massiot, An extension of the Czjzek model for the distributions of electric eld gradients in disordered solids and an application to NMR spectra of ^{71}Ga in chalcogenide glasses, J. Phys. Condens. Matter 22 (2010) 1–17 065402.
[74] C. Legein, J.Y. Buzaré, J. Emery, C. Jacoboni, Electron paramagnetic resonance determination of the local field distribution acting on Cr^{3+} and Fe^{3+} in transition metal fluoride glasses (TMFG), J. Phys. Condens. Matter 7 (1995) 3853–3862.
[75] C. Legein, J.Y. Buzaré, G. Silly, C. Jacoboni, The local field distribution of Gd^{3+} in transition metal fluoride glasses investigated by electron paramagnetic resonance, J. Phys. Condens. Matter 8 (1996) 4339–4350.
[76] H. Daubric, R. Berger, J. Kliava, G. Chastanet, O. Nguyen, J.-F. Létard, Light-induced excited spin-state trapping of Fe^{2+} observed by electron paramagnetic resonance of Mn^{2+}, Phys. Rev. B66 (2002) 1–8 054423.
[77] M. Qian, L. Li, H. Li, D.M. Strachan, Partitioning of gadolinium and induced phase separation in sodium-aluminoborosilicate glasses, J. Non-Cryst. Solids 333 (2004) 1–15.
[78] L. Li, H. Li, M. Qian, D.M. Strachan, Gadolinium solubility in peralkaline borosilicate glasses, J. Non-Cryst. Solids 283 (2001) 237–245.
[79] H. Li, Y. Su, L. Li, M. Qian, D.M. Strachan, Raman spectroscopic study of gadolinium (III) in sodium-aluminium–borosilicate glasses, J. Non-Cryst. Solids 292 (2001) 167–176.
[80] A. Kumar, S.B. Rai, D.K. Rai, Effect of thermal neutron irradiation on Gd^{3+} ions doped oxy-fluoroborate glass: an infra-red study, Mater. Res. Bull. 38 (2003) 333–339.
[81] M. Wang, J. Cheng, M. Li, F. He, Structure and properties of soda lime silicate glass doped with rare earth, Physica B 406 (2011) 187–191.